Received: 24 January 2022 | Revised: 20 May 2022 | Accepted: 26 May 2022

DOI: 10.1002/er.8233

RESEARCH ARTICLE

INTERNATIONAL JOURNAL OF ENERGY RESEARCH WILEY

Numerical simulation of the polymer electrolyte membrane fuel cells with intermediate blocked interdigitated flow fields

Fatemeh Bagherighajari[1] | **Abbas Ramiar**[2] | **Mohammadmahdi Abdollahzadehsangroudi**[3,4] | **José Carlos Páscoa**[4] | **Paulo J. Oliveira**[4]

[1]Department of Mechanical Engineering, Mazandaran University of Science and Technology, Babol, Iran

[2]Department of Mechanical Engineering, Babol Noushirvani University of Science and Technology, Babol, Iran

[3]Faculty of Mechanical of Engineering, University of Guilan, Rasht, Iran

[4]Departamento de Engenharia Eletromecânica, C-MAST – Center for Mechanical and Aerospace Sciences and Technologies, Universidade da Beira Interior, Covilhã, Portugal

Correspondence
M. Abdollahzadeh, Departamento de Engenharia Eletromecânica, C-MAST – Center for Mechanical and Aerospace Sciences and Technologies, Universidade da Beira Interior, Covilhã, Portugal.
Email: mm.abdollahzadeh@ubi.pt

Funding information
Fundação para a Ciência e a Tecnologia, Grant/Award Numbers: CEECIND/03347/2017, UIDB/00151/2020

Summary

The main purpose of this paper is to study fuel cell performance using an interdigitated flow field with intermediate channel blocks on the cathode side. Application of an intermediate block in the middle of the interdigitated flow channel is a very new idea aimed at increasing the performance of polymer membrane fuel cells, which in practice result in novel arrangements of interdigitated flow channels. A middle block is desirable because the change in flow channel is minimal, the cost of fabricating bipolar plates does not increase, and it leads to an increase in the transfer rate of reactants into the gas diffusion layer due to enhanced over-rib flow pattern and direction. In this work, a three-dimensional, isothermal, and two-phase model is used to simulate the performance of such fuel cells. The polarization curves, the distribution of reactants on the cathode side, the distribution of liquid water, and the induced transverse flow were analyzed for three type of interdigitated flow fields along with parallel flow fields at reference conditions. The results showed that interdigitated flow fields with middle blocks lead to an increase in reactant transfer to the catalyst layer, an increase in reaction rate, and better removal of the resulting liquid water within the fuel cell. In the reference condition, in terms of maximum power density, the type I interdigitated flow field (without intermediate block) increased the net power by 8.2% compared to the parallel flow field, and the type II and III interdigitated flow fields also increased the power by 12.58% and 9.03%, respectively. At high current density, the type II interdigital flow field had the best performance in terms of enhancing the transfer of reactants to the catalyst layer and the expulsion of liquid water from that layer.

KEYWORDS

interdigitated flow field, PEM fuel cell, performance enhancement, polarization curve, simulation

1 | INTRODUCTION

Polymer electrolyte membrane fuel cells (PEMFCs) are considered one of the most promising clean energy sources that can help fighting climate change. However, the commercialization of these systems still faces the fundamental challenges of cost reduction, competitiveness, higher power density, and better fuel economy. To improve the performance of fuel cells and reduce the cost of PEMFCs, an optimized design of these systems is required. The necessary improvement in the performance of these fuel cells can be achieved by reducing the existing losses within the fuel cell. Over the years, many researchers have attempted to reduce the concentration losses in fuel cells to achieve higher performance.[1] One of the best strategies to reduce the concentration losses and to cope with the flooding phenomenon in fuel cells and to achieve higher performance is to properly design the patterns and geometric arrangement of the flow channels.[2]

The gas channels in the bipolar plates have the function of providing uniform transfer of the reactant gases to the active surface of the electrode and removing the liquid water from the fuel cell to prevent flooding with minimal pressure drop.[3] The uniform distribution of reactants in catalyst layer (CL) leads to a more uniform current density, higher output power density, better fuel consumption, and lower concentration losses in the fuel cell.[4] Arvay et al[5] considered four important factors in the design of fuel cell flow channels: uniform distribution of reactants in the triple-phase zone to avoid hot spots; removal of accumulated liquid water to facilitate the transfer of reactants to the triple-phase zone; contact surface between the bipolar plates and the gas diffusion layer (GDL) to facilitate electron transfer; and low pressure drop to improve the net performance of the fuel cell. Considering the above criteria, it is clear that flow channel design will be a major challenge.

Among the various flow field patterns used for PEMFC flow channels, the interdigitated flow channel has a special feature.[6] It consists of flow channels that are blocked at the end, so that the reactants are forced to pass through the porous layers (GDL and CL) under the pressure difference between the adjacent channels to reach the outlet.[7] This flow field design increases the mass transfer and water removal rate compared to a parallel flow channel.[8] Ding et al[9] performed a two-phase numerical simulation to compare and evaluate the performance of PEMFCs with parallel, interdigitated, and serpentine flow fields when the walls of the flow channels were straight or wavy. Jian et al[10] performed a steady three-dimensional simulation to investigate the effect of relative humidity on the temperature distribution in the membrane of a PEMFC with an interdigitated flow field. They looked to the changes in current density and temperature when the relative humidity varied between 0% and 100%. Cooper et al[11] experimentally investigated the geometric dimensions of the cathode flow channel and flow stoichiometry on the performance of PEMFCs with parallel and interdigitated flow channels.

Despite the many advantages of interdigitated flow fields, the performance of such a flow arrangement can be further improved with very minor geometric changes. Numerous geometric corrections have been made to conventional flow channels, including hybrid flow fields, angling the channel, changing the curvature of the channel, changing the ratio of rib-to-channel width, changing the channel cross-section, and adding blocks or baffles within the channels. These geometric corrections are mainly responsible for inducing a forced convection mechanism due to the over-rib flow to alleviate the mass transfer problem as well as the accumulation of liquid water in the areas under the walls of the flow channels (called ribs).[12] These areas do not share a common contact surface with the flow of reactants, so the transfer of reactants and the discharge of liquid water in these areas is much more limited. To induce transverse forced convection on the rib (over-rib convection), a special design of flow channels is usually used to create a local pressure difference between adjacent flow channels. The geometry of the flow channels, that is, there width, depth, and shape, tends to influence the over-rib convection.[13] Kanezaki et al[14] used a 2D model to study the effect of over-rib convection on fuel cell performance. Their results showed that enhanced flow convection within the electrodes would increase the concentration of reactants in the CL and improve water removal. Jiao et al[15] conducted a 3D simulation to examine the effects of forced over-rib convection on the flow patterns and performance of the fuel cell. Their results showed that by increasing the pressure difference between high- and low-pressure channels, liquid water and oxygen are more evenly distributed in the CL and the transfer of liquid water out of the fuel cell is facilitated.

Blocking flow channels is known to be a simple and inexpensive method to create or enhance convection over the ribs.[16] Different geometric shapes can be chosen to create blocks in the flow channels, and these barriers can also partially or completely block these channels.[17] Partial blocking of flow channels (so-called indentation) with trapezoidal, semicircular, and square barriers has been performed in cathode flow channels.[18] These indentations in the flow channels increased the amount of reactant in the CL and also the output current density due to enhanced convection and diffusion mechanisms. Heidary et al[19] simulated the effects of parallel and zigzag arrangements of blocks in the channels of a PEMFC. Their results showed that the zigzag arrangement

increased the fuel cell performance by 11% compared to the reference case, and the parallel arrangement of obstacles increased the fuel cell performance by 7%. Li et al[20] used a genetic algorithm optimization method and three-dimensional simulations to optimize the partial blockage of the cathode parallel flow channel of the PEMFC and found that the net power of the fuel cell is increased by 10.9% with optimal configuration. Recently, Yan et al[21] and Thitakamol et al[22] experimentally investigated new arrangements of interdigitated flow fields using an intermediate square block in the flow channels. They found that the placement of a middle block in the channels of an interdigitated flow field improves the over-rib convection characteristics of this flow field and thus the performance of the fuel cell. They proposed two new types of interdigitated flow fields (interdigitated flow field type II and type III), depending on how this intermediate block is placed in the flow channel.

Among conventional flow fields, the interdigitated flow field has received much attention because of its enhanced over-rib convection mechanism. Literature shows that there is no theoretical study and computational fluid dynamics simulation of PEMFC with intermediate blocked arrangements of interdigitated flow fields (Type II, III) compared to conventional interdigitated flow fields (Type I). Therefore, the main objective is to simulate and compare the performance of different types of interdigitated flow channels (Type I, II, and III) generated by placing an intermediate block in the flow channel (see Figure 1). The specific goal is to analyze the mechanisms responsible for the performance improvement of these new flow fields. This article is divided into five sections. In this first section, an introduction and a literature review are given. In Section 2, the definition of the problem is described in detail. In Section 3, the governing equations for the problem, boundary conditions, and other aspects of the mathematical model are given and discussed. In Section 4, the numerical simulation method is briefly outlined and finally, in Section 5, the main results of this study are stated and compared with previous related research, and are commented and put into perspective in terms of their consequences.

2 | PROBLEM DEFINITION

The main objective of this paper is to analyze a new interdigitated flow channel arrangement using an intermediate block for PEMFCs. Figure 1 shows a schematic of parallel and interdigitated flow channel and two new types of interdigitated flow channels with midblock.

Figure 1A shows the parallel flow channel and the corresponding arrangement of the computational grid is shown in Figure 2C. The geometric feature of this channel is that there is an outlet for each inlet. Due to this geometric feature, the reactants are uniformly distributed in the CL. In addition, the pressure drop Δp (defined as the pressure difference between inlet and outlet) in this flow channel is low. Due to the low pressure drop and the absence of velocity components (convection effects) in the GDL, mass transport and flooding problems can occur normally in this flow channel. Figure 1B shows a schematic of an interdigitated flow channel (type I). In this flow arrangement, the inlets are alternately closed and the outlets are also alternately arranged. In this way, the channel that has an inlet has no outlet and the channel that has an outlet has a closed inlet. Due to this particular geometric arrangement, the reactant gases move from one channel to the adjacent channel by a forced convection mechanism or, in other words, by the over-rib convection through the GDL. The over-rib convection increases the concentration of reactants in the CL compared to the parallel flow field. It also removes and expels liquid water that has accumulated in the GDL in the region below the rib. The geometric arrangement of the interdigitated flow channel increases the pressure difference between the inlet and outlet of the channel. Although convection over the ribs can increase fuel cell performance at the expense of a higher pressure drop, it also increases pumping power, which reduces the resulting net fuel cell performance. Figure 1C shows a schematic of an interdigitated flow channel arrangement (type II) that uses an intermediate block. The geometric feature of this flow channel is that, given a pair of adjacent channels, one of these channels has an inlet and an outlet with an intermediate block and the other channel has no inlet or outlet. As can be seen in the figure, this arrangement, similar to an interdigitated flow channel (type I), results in convection of the reactants over the ribs. Thus, it has similar advantages to the interdigitated flow channel (type I), but because of the particular arrangement of this flow channel, the over-rib convection of the reactants occurs in a zigzag pattern. Figure 1D shows another new arrangement of the interdigitated flow channel (type III) with the intermediate block. The geometric feature of this flow arrangement is that one channel has an inlet whose outlet is blocked, and the adjacent channel has an inlet and an outlet with an intermediate block. In this channel, which is similar to the channel shown in Figure 1C, convection takes place over the ribs in a zigzag pattern.

3 | GOVERNING EQUATIONS

To simulate a PEMFC, the various physical phenomena that occur in it must be represented by a mathematical model. These physical phenomena in a PEMFC include:

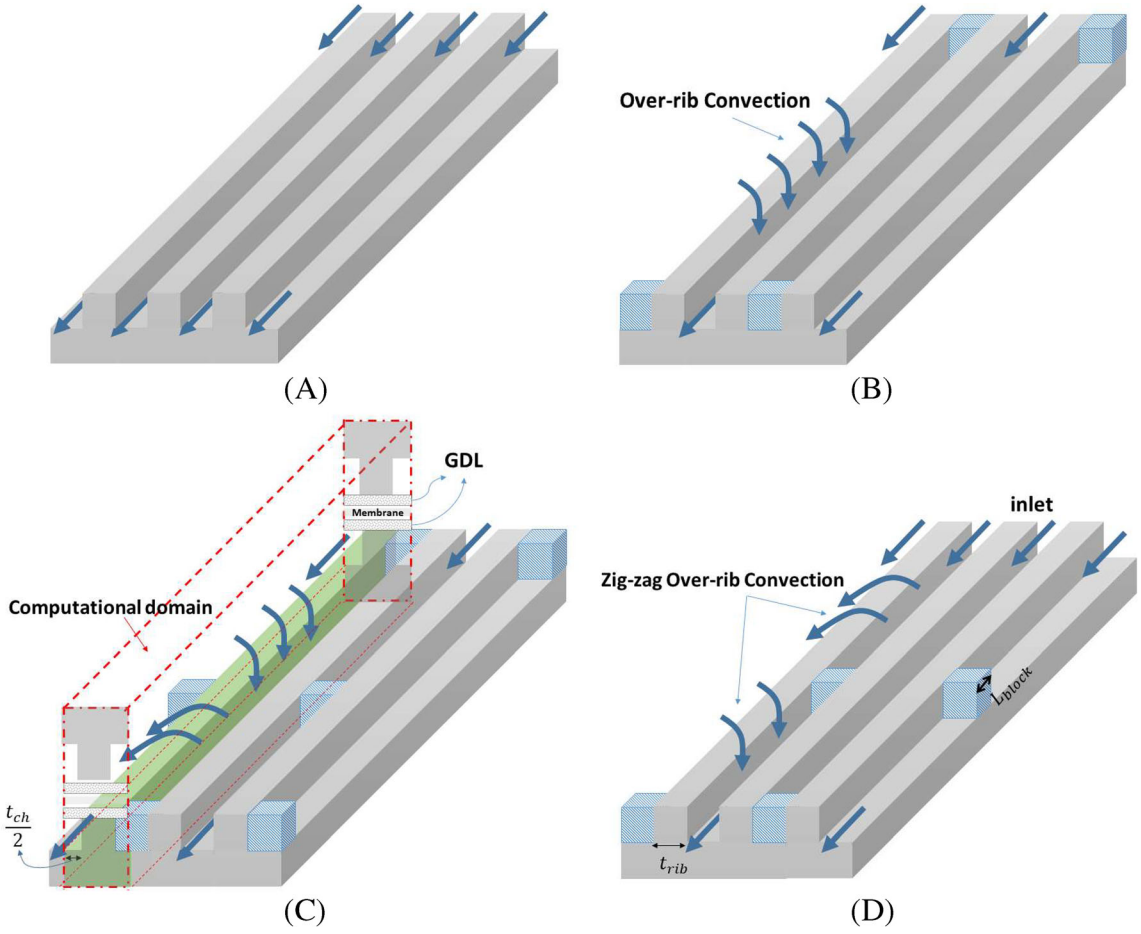

FIGURE 1 Schematic of the gas flow channels in the cathode side simulated in the present study: (A) Parallel flow field; (B) Interdigitated flow field (type I); (C) Interdigitated flow field with middle block (type II); (D) Interdigitated flow field with middle block (type III)

Multicomponent transport phenomena of gaseous species, including oxygen, hydrogen, and nitrogen; transfer of different water phases, including water vapor, water dissolved in membranes, and liquid water; phase changes between different water phases; the kinetics of electrochemical reactions; and the transfer of electric charge and energy. The mathematical model used in this work is established on the following general assumptions:

- The gas mixture is assumed to behave like an ideal gas.
- A steady and laminar flow is assumed.
- The influence of gravity is ignored.
- It is assumed that the fuel cell operates under isothermal conditions.

It should be mentioned that the isothermal assumption is based on the fact that in most laboratory tests of a single cell (not a stack) fuel cell, temperature variations are tightly limited using PID controllers and heating units.[24] In such a case, the temperature variation within the fuel cell is small and can be ignored, as shown by Zamel and Li.[25] Hence, the assumption of isothermal conditions in the current investigation should still result in accurate estimation of the fuel cell performance. Steady state and laminar flow regime assumptions are based on the following facts: the maximum Reynolds number of flow is less than 2100; the reactants are supplied steadily to the fuel cell and a constant current is extracted from the cell. Gravity is also assumed to be negligible since in this way the analysis may be solely focused on the variation of flow fields. The drag force imparted to the water droplets by the gas flow inside the channels is much more significant than gravity due to the small size of liquid water droplets and the low concentration of liquid water in the gas channels.The governing equations of the PEMFC are given in Table 1.

In the above equations, ρ_g, $\vec{u}_g$, p_g, S, and ε represent density, velocity, gas phase pressure, liquid water saturation ($S = V_l/V_{\text{pore}}$), and porosity coefficient, respectively. τ is the viscous stress tensor, S_m and S_u represent the sources/sinks in the continuity and momentum equations, respectively. Assuming that the fuel cell is supplied

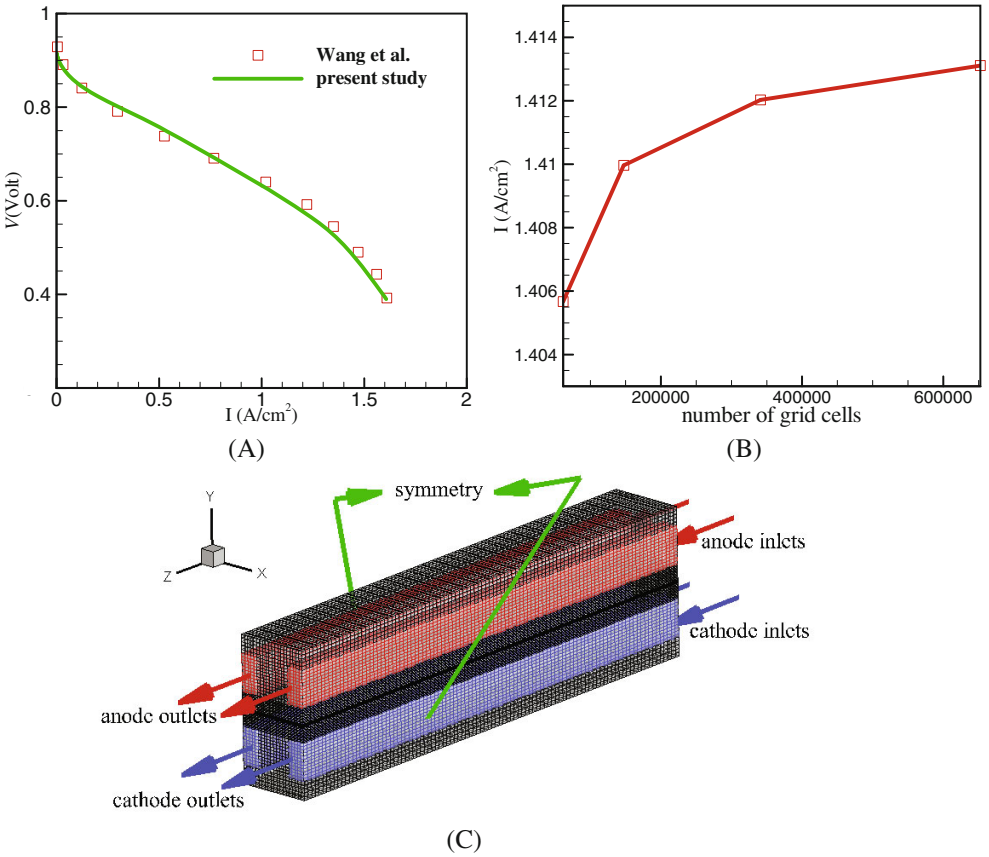

FIGURE 2 (A) Comparison of simulated polarization curve of PEMFC on the base grid with the experiments of Wang et al,[23] (B) Check of grid independence in terms of output current density at a constant voltage of 0.5 V, and (C) Schematic of fuel cell geometry and the corresponding computational grid for validation

TABLE 1 Equations governing the mathematical model of a PEMFC

Description	Equations	
Gas mixture continuity equation:	$\frac{\partial}{\partial t}\left(\varepsilon(1-S)\rho_g\right)+\nabla\cdot\left(\rho_g\vec{u}_g\right)=S_m$	(1)
Gas mixture momentum equation:	$\frac{\partial}{\partial t}\left(\frac{\rho_g\vec{u}_g}{\varepsilon(1-S)}\right)+\nabla\cdot\left(\frac{\rho_g\vec{u}_g\vec{u}_g}{\varepsilon^2(1-S)^2}\right)=-\nabla p_g+\nabla\cdot\bar{\bar{\tau}}+S_u$	(2)
Mass conservation equation for each species:	$\frac{\partial\left((1-S)\rho_g Y_k\right)}{\partial t}+\nabla\cdot\left(\rho_g\vec{u}_g Y_k\right)=\nabla\cdot\left(\rho_g D_k^{eff}\nabla Y_k\right)+S_k$ $k=H_2;O_2;H_2O;N_2$	(3)
Electron transport equation:	$\nabla\cdot(\sigma_{sol}\nabla\phi_{sol})+R_{sol}=0$	(4)
Proton transport equation:	$\nabla\cdot(\sigma_{mem}\nabla\phi_{mem})+R_{mem}=0$	(5)
Transport of dissolved water in membrane:	$\frac{\partial}{\partial t}\left(\frac{\varepsilon_{mem}M_{H_2O}\rho_{mem}\lambda}{EW}\right)+\nabla\cdot\left(\frac{\vec{i}_{mem}n_dM_{H_2O}}{F}\right)=\nabla\cdot\left(M_{H_2O}D_w^{mem}\nabla\lambda\right)+S_\lambda+S_{gd}+S_{ld}$	(6)
Liquid water transport equation in porous media:	$\frac{\partial}{\partial t}(\varepsilon S\rho_l)=\nabla\cdot\left(\varepsilon\rho_l\frac{K_rK}{\mu_l}\nabla\left(p_c+p_g\right)\right)+S_{gl}-S_{ld}$	(7)
Liquid water transport in gas channels:	$\frac{\partial}{\partial t}(S\rho_l)+\nabla\cdot\left(\rho_l\chi\vec{u}_gS\right)=\nabla\cdot\left(D_{liq}\nabla S\right)$	(8)

with humidified air and hydrogen, four gaseous components are considered in the model: Hydrogen, Oxygen, Water Vapor, and Nitrogen. For these gaseous species, it is only necessary to solve Equation (3) for three of them, and the mass fraction of the last chemical species can be obtained from the equation $\sum_k Y_k=1$. In Equation (3), Y_k,, D_k^{eff}, and S_k denote the mass fraction, the effective diffusion coefficient,[26] and the source/sink term related to the consumption or production rate of chemical species k, respectively.

TABLE 2 Description of the source/sink terms

Description	Equations	
Continuity equation source/sink term:	$S_m = \sum_k S_k = S_{H_2} + S_{O_2} + S_{H_2O}$	(9)
Momentum sink term due to effect of porous media:	$S_u = -\frac{\mu_g}{K}\vec{u}_g$	(10)
The rate of consumption of species in electrochemical reaction:	$S_{H_2} = -\frac{M_{H_2}R_{an}}{2F}; S_{O_2} = -\frac{M_{O_2}R_{ca}}{4F}; S_{H_2O} = -S_{gl} - S_{gd}$	(11)
Production rate dissolved water in electrochemical reaction:	$S_\lambda = \frac{M_{H_2O}R_{ca}}{2F}$	(12)
Vapor to dissolved water phase change rate[33]:	$S_{gd} = (1 - S^\theta)\gamma_{gd}M_{H_2O}\frac{\rho_{mem}}{EW}(\lambda_{equil} - \lambda)$	(13)
Liquid to dissolved water phase change rate[33]:	$S_{ld} = S^\theta\gamma_{ld}M_{H_2O}\frac{\rho_{mem}}{EW}(\lambda_{equil} - \lambda)$	(14)
The phase change rate during evaporation/condensation process:	$S_{gl} = \begin{cases} \frac{\gamma_e\varepsilon SD_{gl}M_{H_2O}}{RT}\text{pln}\left(\frac{p-p_{sat}}{p-p_{wv}}\right) \; if\; p_{wv} \le p_{sat} \\ \frac{\gamma_c\varepsilon(1-S)D_{gl}M_{H_2O}}{RT}\text{pln}\left(\frac{p-p_{sat}}{p-p_{wv}}\right) \; if\; p_{wv} > p_{sat} \end{cases}$	(15)
Electronic exchange current density:	$R_{sol} = \begin{cases} -R_{an}(<0) \text{ in ACL} \\ +R_{ca}(>0) \text{ in CCL} \end{cases}$	(16)
Protonic exchange current density:	$R_{mem} = \begin{cases} +R_{an}(>0) \text{ in ACL} \\ -R_{ca}(<0) \text{ in CCL} \end{cases}$	(17)

In the PEMFC, water is present under three phases: dissolved, liquid, and gas (water vapor). The simultaneous presence of three water phases in the CL causes different phase change processes. Equation (6) describes the transfer of dissolved water in the electrolyte of the CL and the membrane.[27] This equation also implies that water can be transported in the polymer membrane due to diffusion and electroosmotic drag. In this equation, ε_{mem} denotes the volume fraction of the electrolyte, D_w^{mem} is the effective diffusion coefficient of dissolved water in the membrane, n_d is the electroosmotic drag coefficient,[28] $\vec{i}_{mem}$ is the ionic current density in the membrane phase ($\vec{i}_{mem} = -\sigma_{mem}\nabla\phi_{mem}$; σ_{mem} = protonic conductivity, ϕ_{mem} = electric potential in membrane phase). The transport of liquid water within the porous regions is described by Equation (7). In this equation, K and K_{rl} represent the absolute permeability of porous media and the relative permeability of liquid. At the GDL/channel interfaces, the flux of water is possible only into the flow channels, without the possibility of reversing the direction of such flux, which is obtained according to the capillary pressure. In Equation (8), D_{liq} represents the diffusion coefficient for liquid water in the flow channels and χ represents the ratio of the flow velocity of the liquid to the flow velocity of the gas. In practice, we assume that the liquid water is transported at a similar velocity as the gas flow and the value of χ becomes equal to one. In this case, the diffusion coefficient D_{liq} takes a large value to satisfy the assumption of uniform mist flow.[29] The electrochemical model is based on studies by Kulikovsky et al,[30] Mazumder and Cole,[31] and Um et al,[32] in which two equations, Equations (4) and (5), are considered for electrochemistry. In these equations, σ_{sol} and σ_{mem} are the electron and proton conductivities[28]; ϕ_{mem} and ϕ_{sol}, the electric potentials, and R_{sol} and R_{mem}, the volumetric exchange current densities.

The source/sink terms in Equations (1) to (8) are given in Table 2. In Equation (1), S_m includes the effects of phase change and electrochemical reactions that cause mass production and consumption. In Equation (3), S_k is the source/sink for the effects of electrochemical reaction of gaseous species (oxygen consumption, hydrogen consumption) and mass transfer between vapor/liquid water and vapor/dissolved water. In Table 2, Darcy's law for porous materials is used to express the S_u in the momentum equation (Equation [2]) and Equation (10) gives the resistance to the flow when passing through a porous material, K being the absolute permeability of porous media. This source S_u has nonzero values only in porous media, which include gas diffusion and catalyst layers, whereas in the gas channels, the value of S_u is set to zero. The R_{sol} and R_{mem} in Equations (4) and (5) are the exchanged current densities, expressing the rate of electrochemical reaction (rate of production/consumption of

electrons/protons), and take a non-zero value only in the reaction zone (CL).

In Equations (16) and (17), the values of R_{an} and R_{ca} in the anode and cathode catalyst layers (ACL and CCL) are calculated from the Butler–Volmer equation:

$$R_{an} = (1-S)^{\gamma_j}\left(a_{pt,an} j_{an}(T)\right)\left(\frac{C_{H_2}}{C_{H_2,\mathrm{ref}}}\right)^{\gamma_{an}}\left(e^{\frac{\alpha_{an}^{an} F \eta_{an}}{RT}} + e^{-\frac{\alpha_{ca}^{an} F \eta_{an}}{RT}}\right), \tag{18}$$

$$R_{ca} = 4F\frac{C_{O_2}}{\frac{C_{O_2}}{j_{O_2}^{\mathrm{ideal}}} + \mathfrak{R}_{\mathrm{ion}} + \mathfrak{R}_{\mathrm{liq}}}. \tag{19}$$

In Equation (19), a cathode agglomerate, or particle model, is used to simulate the electrochemistry governing the cathode catalyst layer. This model considers that the resistance to mass transfer in the catalytic layer[34] is due to the agglomeration of platinum particles together with the carbon base and these agglomerates are connected to each other by the ionomer and the structure of the GDL. The agglomerates are spheres of electrolyte, usually Nafion, which are filled with carbon and platinum particles and have a radius of about one micron.[35] In the literature, it is commonly assumed that these particles are similar, have a spherical shape, and are separated by empty space. In Equation (19), $\mathfrak{R}_{\mathrm{ion}}$ and $\mathfrak{R}_{\mathrm{liq}}$ are the extra mass transfer resistances in the CL.[36] A specific value is usually considered for $\mathfrak{R}_{\mathrm{ion}}$ and the value of $\mathfrak{R}_{\mathrm{liq}}$ is calculated from the following Equation[33]:

$$\mathfrak{R}_{\mathrm{liq}} = \frac{a_{pt,ca} r_{\mathrm{agg}}^2}{K_w D_w}\frac{\sqrt[3]{1+\frac{S\varepsilon}{1-\varepsilon}}}{3(1-\varepsilon)}. \tag{20}$$

In the above equation, the product of $K_w D_w$ represents the solubility of oxygen in liquid water. In Equation (19), the value of $j_{O_2}^{\mathrm{ideal}}$ is calculated as:

$$j_{O_2}^{\mathrm{ideal}} = \frac{(1-S)^{\gamma_j}\left(a_{pt,ca} j_{ca}(T)\right)\left(\frac{C_{O_2}}{C_{O_2,\mathrm{ref}}}\right)^{\gamma_{ca}}\left(-e^{\frac{\alpha_{an}^{ca} F \eta_{ca}}{RT}} + e^{-\frac{\alpha_{ca}^{ca} F \eta_{ca}}{RT}}\right)}{4F}. \tag{21}$$

In Equations (21) and (18), $j(T)$ is the reference transfer current per unit area as a function of temperature, and a_{pt} represents the effective specific surface area. In Equation (18), the effects of liquid water accumulation in the CL are considered as an additional resistance that reduces the electrochemical active surface area, C and C_{ref} express the values of the local molar concentration of the reactants and the reference molar concentration, respectively. Moreover, in the above equations, γ is the concentration function of the exchange current density, α_{an}^{an} and α_{ca}^{an} represent the reaction transfer coefficients on the anode side and α_{an}^{ca} and α_{ca}^{ca} the transfer coefficients on the cathode side. Finally, F is the Faraday constant, R is the universal gas constant, T is the absolute temperature, and η_{an} and η_{ca} are the surface overpotentials in the anode and cathode catalyst layers. Other parameters and transfer properties in the governing equations can be found in Table 3.

3.1 | Boundary conditions

The mathematical model described above can be solved using either a multi-domain or a single-domain approach. In this work, the single-domain approach is followed so that it is not necessary to define the boundary conditions between the different regions and all governing equations are solved throughout the computational space. Therefore, only the boundary conditions at the outer boundaries need to be defined:

- At the anode and cathode, and at the cathode inlets, the input mass flow rates are defined based on stoichiometric coefficients and a reference current, usually the output current of the fuel cell (A = are of the membrane electrode assembly):

$$\dot{m}_{\mathrm{in},ca} = \frac{\xi_{ca} M_{O_2} I A}{4 Y_{O_2}}; \dot{m}_{\mathrm{in},an} = \frac{\xi_{an} M_{H_2} I A}{2 Y_{H_2}}. \tag{40}$$

- The mass fractions of all species at the inlet are given; at the cathode inlet:

$$Y_{O_2,\mathrm{in}} = 0.21\left(\frac{p_{ca}}{RT} - RH\frac{p_{\mathrm{sat}}}{RT}\right)\frac{M_{O_2}}{\rho_g}, \tag{41}$$

$$Y_{H_2O,\mathrm{in}} = \left(RH\frac{p_{\mathrm{sat}}}{RT}\right)\frac{M_{H_2O}}{\rho_g}. \tag{42}$$

- and at the anode inlet:

$$Y_{H_2,\mathrm{in}} = \left(\frac{p_{an}}{RT} - RH\frac{p_{\mathrm{sat}}}{RT}\right)\frac{M_{H_2}}{\rho_g}, \tag{43}$$

TABLE 3 Transfer parameters of the PEMFC model

Description	Equation	
Density of gas mixture:	$\rho_g = p_g\left(RT\sum_k \frac{Y_k}{M_k}\right)^{-1}$	(22)
Temperature dependence of the reference anode current density:	$j_{an}(T) = j_{an}^{\text{ref}}\, e^{-\frac{E_{an}}{RT\left(1-\frac{T}{T_{an}^{\text{ref}}}\right)}}$	(23)
Temperature dependence of the reference cathode current density:	$j_{ca}(T) = j_{ca}^{\text{ref}}\, e^{-\frac{E_{ca}}{RT\left(1-\frac{T}{T_{ca}^{\text{ref}}}\right)}}$	(24)
Surface over potential in anode catalyst layer:	$\eta_{an} = \phi_{\text{sol}} - \phi_{\text{mem}}$	(25)
Surface over potential in CCL:	$\eta_{ca} = \phi_{\text{sol}} - \phi_{\text{mem}} - V_{oc}$	(26)
Leveret function:	$J(s) = \begin{cases} 1.417(1-S) - 2.120(1-S)^2 + 1.263(1-S)^3 \ \theta_c < 90 \\ 1.417S - 2.120S^2 + 1.263S^3 \ \theta_c > 90 \end{cases}$	(27)
Surface tension of liquid water:	$\sigma = -0.167591 \times 10^{-3}\max(273.15, T) + 0.121836$	(28)
Rate constant of the evaporation/condensation phase change process:	$D_{gl} = \begin{cases} 0.365 \times 10^{-4}\left(\frac{T}{343}\right)^{2.334}\left(\frac{10^5}{p}\right) \text{ if cathode side} \\ 1.79 \times 10^{-4}\left(\frac{T}{343}\right)^{2.334}\left(\frac{10^5}{p}\right) \text{ if anode side} \end{cases}$	(29)
Water activity:	$a = \frac{p_{wv}}{p_{\text{sat}}} = \frac{RT}{p_{\text{sat}}} C_{\text{H}_2\text{O}}$	(30)
Equilibrium water content:	$\lambda_{\text{equil}} = 0.36 + 6a(1 - \tanh(a - 0.5)) + 0.69(\lambda_{a=1} - 3.52)a^{0.5}\left(1 + \tanh\left(\frac{a-0.89}{0.23}\right)\right) + S(\lambda_{S=1} - \lambda_{a=1})$	(31)
Relative permittivity of liquid:	$K_{rl} = S^3$	(32)
Capillary pressure:	$p_c = \sigma\cos(\theta_c)\sqrt{\left(\frac{\varepsilon}{K}\right)}J(S)$	(33)
Effective diffusion coefficient:	$D_k^{\text{eff}} = \varepsilon^{1.5}(1-S)^{2.5}D_k$	(34)
Protonic conductivity of membrane:	$\sigma_{\text{mem}} = \Gamma_i(0.514\lambda - 0.326)^{\omega_i} e^{1268\left(\frac{1}{303} - \frac{1}{T}\right)}$	(35)
Diffusion coefficient of dissolved water in membrane:	$D_w^{\text{mem}} = \frac{\rho_{\text{mem}}}{EW} 4.1 \times 10^{-10}\left(\frac{\lambda}{25}\right)^{0.15}\left[1 + \tanh\left(\frac{\lambda - 2.5}{1.4}\right)\right]$	(36)
Electroosmotic drag coefficient:	$n_d = \frac{2.5\lambda}{22}$	(37)
Saturation pressure of water vapor:	$\log_{10}\frac{p_{\text{H}_2\text{O}}^{\text{sat}}}{101325} = -2.1794 + 0.02953(T - 273.15) - 9.1837 \times 10^{-5}(T - 273.15)^2 + 1.4454 \times 10^{-7}(T - 273.15)^3$	(38)
Diffusion coefficient of species at specified pressure and temperature:	$D_k = D_k^0\left(\frac{T}{T_{\text{ref}}}\right)^{1.5}\left(\frac{p_{\text{ref}}}{p}\right)$	(39)

$$Y_{H_2O,in} = \left(RH\frac{p_{sat}}{RT}\right)\frac{M_{H_2O}}{\rho_g}. \quad (44)$$

- A zero flux boundary condition is imposed for all other variables.
- A constant pressure is set at the outlet boundaries of the anode and cathode channels, and the gradient of the mass fraction of the gaseous components is assumed to be zero. The zero flux condition is also used for other variables:

$$\frac{\partial Y^k}{\partial n} = 0; p_{out} = p_{specified}. \quad (45)$$

- A no-slip condition is assumed for the velocity vector at the wall surfaces.
- At the bipolar plate/flow channel and bipolar plate/GDL interfaces, a coupled boundary condition for the electric potential is used.
- At the outer surfaces of the bipolar plates (terminal surfaces), a boundary condition is required for the electric potential. Such boundary condition expresses the operation of a fuel cell in the galvanostatic or potentiostatic states and is given by:

$$\phi_{sol} = V_{cell} \text{ at cathode if potentiostatic mode,} \quad (46)$$

$$\frac{\partial \phi_{sol}}{\partial n} = -I_{cell} \text{ at cathode if galvanostatic mode,} \quad (47)$$

$$\phi_{sol} = 0 \text{ at anode.} \quad (48)$$

A comment related to this boundary condition is here pertinent: when the stoichiometry is variable (ie, constant mass flow at the inlet), application of a boundary condition for either current or voltage makes no difference. When the mass flow inlet is based on a constant stoichiometry (calculated according to Equation [40]), with a constant potential boundary condition (Equation [46]), an iterative process is required to determine the current and then change the mass flow. In this latter case, a current boundary condition (Equation [47]) is used for simplicity.

4 | NUMERICAL SOLUTION METHOD

Ansys Fluent software was used to simulate the PEM fuel cell.[37] Fluent is based on the finite volume method for solving the governing equations with the applied boundary conditions. As for the discretization methods for the momentum equations and the chemical species, a second-order upwind scheme was employed, while the discretization of the pressure equation follows a standard central scheme. The SIMPLE algorithm was applied to solve the pressure–velocity coupling with under-relaxation coefficients of 0.7, 0.3, and 0.9 for the momentum, the pressure correction, and the chemical species equations.

5 | RESULTS AND DISCUSSIONS

5.1 | Validation

The validation is based on the experimental results of Wang et al,[23] with the geometrical and operating parameters of the fuel cell, for the reference case, given in Table 4. The three-dimensional computational domain corresponding to this geometry of the fuel cell, which consists of only a single rib and two half channels, was created considering the geometric symmetry of the gas channels, giving a computational grid with 147 400 elements. This grid was created by dividing the length of fuel cell channels into 112 elements, channel depth into ten elements, channel width into ten elements, thickness of CL into seven elements, thickness of GDL into ten elements, and thickness of polymer membrane into seven elements. A schematic representation of the fuel cell geometry and the grid used for validation is given in Figure 2C. We should note that the choice for the number of suitable grid elements in the numerical computation was defined after analyzing the independence of the results in relation to grid density. The results of the grid independence study are given in the next section. The values of the parameters used for both the validation and parametric studies are given in Table 4. The values of the parameters for the parametric study and the validation are different. The validation of the work was done against the experimental work of Wang et al[23] and the parametric study was done in a way to replicate the experimental work of Thitakamol et al.[22] It is important to point out that the interdigitated type I flow field was used in the anode side, for all cases here tested, so that a direct comparison was possible against the experimental work of Thitakamol et al.[22]

The polarization curve for the PEMFC obtained with the three-dimensional simulation of the PEM fuel cell is compared against the results of Wang et al[23] in Figure 2a. As seen from the comparison of the current density plotted in the figure, our simulation results are well matched to the experimental results of.[23]

TABLE 4 Structural and operating parameters for validation with experimental results of[23] and reference operating conditions for the parametric study of various fuel cells

Description	symbol	Value for validation	Value in parametric study
Height of gas channel	H_{ch}	1 mm	1 mm
Bipolar plate thickness	H_{bp}	1 mm	0.5 mm
Gas diffusion layer thickness	H_{GDL}	300 μm	410 μm
Catalyst layer thickness	H_{CL}	12 μm	28.7 μm
Membrane thickness	H_{mem}	108 μm	35 μm
Width of gas channel	w_{ch}	1 mm	1 mm
Width of rib	w_{rib}	1 mm	1 mm
Gas channel length	L_{ch}	70 mm	70 mm
Block thickness	L_{block}	-	1 mm
Block height	H_{block}	-	1 mm
Porosity of gas diffusion layer	$\varepsilon_{\mathrm{GDL}}$	0.4	0.6
Hydraulic permeability of gas diffusion layer	K_{GDL}	$1.76\times10^{-11}\,\mathrm{m}^2$	$3\times10^{-12}\,\mathrm{m}^2$
Porosity of catalyst layer	ε_{CL}	0.4	0.2
Hydraulic permeability of catalyst layer	K_{CL}	$1.76\times10^{-11}\,\mathrm{m}^2$	$2\times10^{-13}\,\mathrm{m}^2$
Humidity of the gas mixtures at inlets (Anode and cathode)	RH	100%	100%
Hydrogen inlet stoichiometric flow coefficient (corresponds to reference current of 1 $\mathrm{A/cm^2}$)	$\xi_{\mathrm{H_2}}$	2.98	1.375
Oxygen inlet stoichiometric flow coefficient (corresponds to reference current of 1 $\mathrm{A/cm^2}$)	$\xi_{\mathrm{O_2}}$	2.3	1.393
Operating pressure (reference pressure)	p_{ref}	3 atm	1 atm
Contact angle	θ_c	120°	110°
Operating temperature	T	70°C	80°C
Reference anode current density	$a_{pt,an}j_{an}(T)$	$1.5\times10^{9}\,\mathrm{A/m^3}$	$2\times10^{9}\,\mathrm{A/m^3}$
Reference cathode current density	$a_{pt,ca}j_{ca}(T)$	$2.8\times10^{5}\,\mathrm{A/m^3}$	$4\times10^{5}\,\mathrm{A/m^3}$
Open circuit voltage	V_{oc}	0.93 Volt	0.95 V
Anode and cathode charge transfer coefficient	α_a,α_c	1, 2	0.5, 0.5

5.2 | Analysis of grid independence

To verify the independence of the grid, four computational grids were created with 61 490, 147 400, 341 040, and 652 608 elements. For each grid, the fuel cell output was simulated at a constant voltage of 0.5 V using the parameters from Table 4, and the fuel cell output current density was then calculated. The variation of the output current density obtained from the simulations on these grids is shown in Figure 2B. These results show that the differences between predictions on the different grids tend to diminish, especially as the grids are refined (current density varies from 1.412 to 1.413 for the two most refined grids that is by 0.07%), but it is clear that the differences are small even in the base grid.

To better assess grid independence, a grid convergence index was calculated according to.[38] This grid convergence parameter (GCI) provides an estimate of the amount of error between the finest grid and the numerically converged solution.[39] Such GCI calculated on three meshes having 61 490 (mesh 3), 147 400 (mesh 2), 341 040 elements (mesh 1) and the corresponding results are given in Table 5.

In the above table, GCI_{21} is equal to $F_s e_{21}/\left(r_{21}^{P}-1\right)$, where F_s is a safety factor having a value of 1.25, i and j are indices to identify the grid, h is a measure of grid spacing (total volume divided by the number of elements), r stands for the grid refinement ratio (defined as $r_i = h_i/h_j$), P is order of convergence, and $f^{*} = \left(r_{21}^{P} f_1 - f_2\right)/\left(r_{21}^{P}-1\right)$ is an the estimation of the numerically converged value of the variable of the interest in the GCI analysis (here the current density $I(\mathrm{A/cm^2})$). From the results of Table 5, it can be concluded that the grid with 341 040 elements ensures with

TABLE 5 Calculation of grid convergence index

Mesh number	Number of elements	h(mm)	$r_i = h_i/h_j$	$f_i = I$ (A/cm^2)
3	61 490	0.22088897	2.397	1.405672
2	147 400	0.16504792	2.313	1.409963
1	341 040	0.12478834	-	1.412026
P	0.9413	GCI_{21}	0.92%	f^* 1.423556

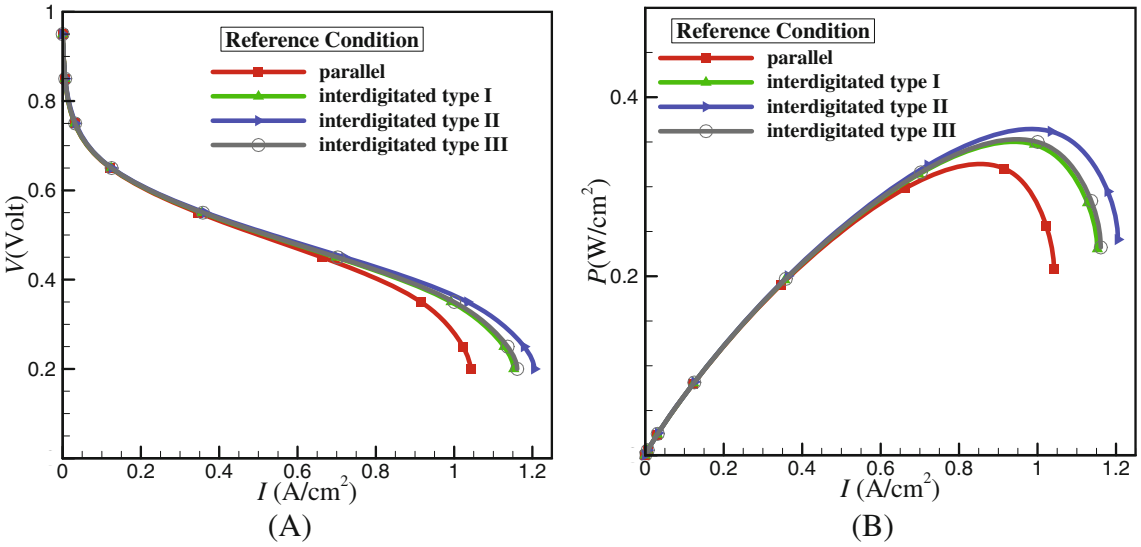

FIGURE 3 (A) Polarization curves (voltage-current density plot) and (B) power density vs current density for fuel cells with parallel, interdigitated type I, type II, and type III flow fields at reference conditions

95% confidence a simulation value in the range [1.40005:1.42617]. When calculating the GCI for mesh 2, the value of this index is equal to 1.25%. Therefore, it can be concluded that using mesh 2 with 147 400 elements, the simulation value is in the range [1.39297:1.426955] with 95% confidence. On the basis that mesh 2 is favorable in terms of GCI and also because it requires shorter runtimes, mesh 2 with 147 400 elements is selected as the grid that provides grid-independent results at a reasonable runtime.

5.3 | Comparison of performance of fuel cells with different flow fields at reference conditions

In this section, a detailed and comprehensive analysis of the performance of fuel cells with parallel, interdigitated flow fields of type I, type II, and type III (see Figure 1) is performed under the reference conditions. The reference conditions include the specification of inlet anode and cathode mass flows, inlet relative humidity, operating temperature, and pressure; these correspond to the conditions of the experimental work by Thitakamol et al,[22] and the corresponding values are given in Table 4. The various geometric dimensions, such as thickness (L_{block}) and height (H_{block}), used to produce the interdigitated blocks are also given in Table 4. For the reference conditions, a constant inlet mass flow rate is assumed for the anode and cathode. For each of the cathode flow fields, the fuel cell performance is modeled at constant operating voltages and the corresponding polarization curves obtained from the numerical simulations are shown in Figure 3. Up to a current density of about 0.6 A/cm^2, fuel cells with different flow fields show the same performance. This result is consistent with those previously published in the literature. At low current densities, the consumption rate of reactants in the CL is low and consequently the rate of water vapor production and liquid water formation in the fuel cell is also low. In this case, the effects of concentration losses are negligible, so all fuel cells have the same performance. However, as the current density is increased, the reaction rate and liquid water accumulation in the fuel cell should also increase, and the fuel cell using the parallel flow channel has the lowest performance compared with other fuel cells. The reason is that all types of interdigitated flow fields introduce the forced convection mechanism in addition to the diffusion mechanism to transport the reactants and remove the liquid water. Among the various types of

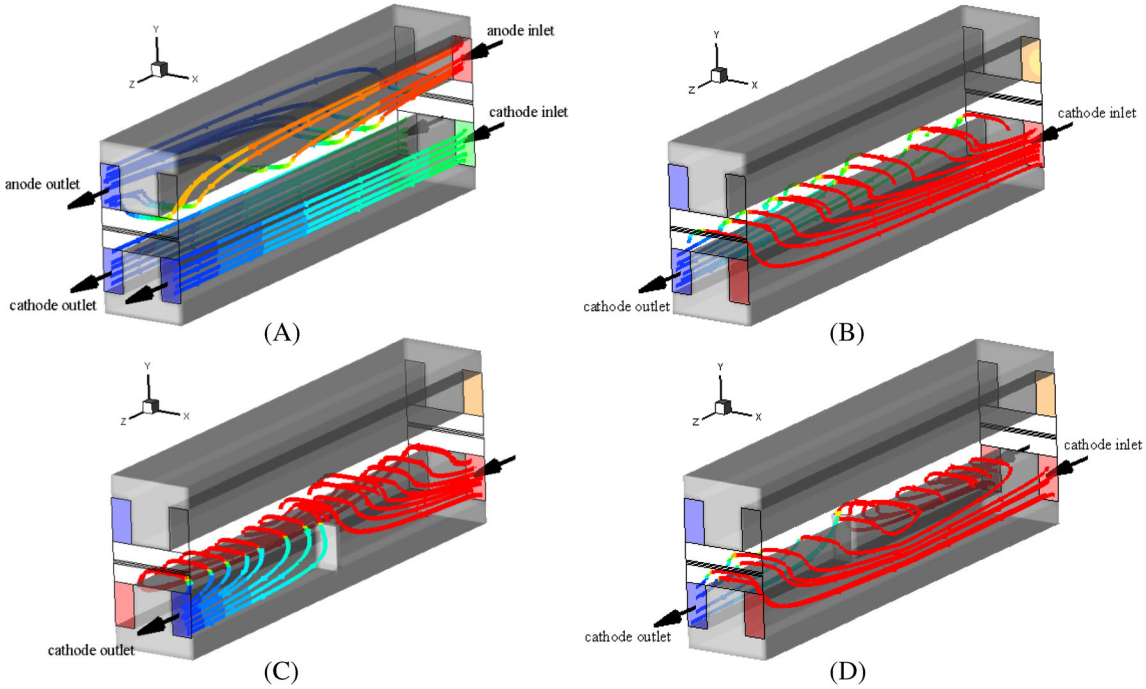

FIGURE 4 Streamlines in fuel cell flow channels with the flow fields: (A) parallel; (B) Interdigitated type I; (C) type II; (D) type III

interdigitated flow fields, the type II flow channel is seen to achieve the highest performance. The performance of the type III is also slightly improved compared to the type I interdigitated flow channel.

To better understand the differences in the mechanisms of the various flow channels on fuel cell performance, the flow streamlines in the anode and cathode flow channels are shown in Figure 4. As can be seen in Figure 4A, the anode flow channel is of the interdigitated type I. For this reason, the flow coming from the anode inlet flows across the anode GDL and reaches the anode outlet. The color of the streamlines in this figure indicates the pressure values. The interdigitated flow channel on the anode side causes a pressure gradient between two adjacent channels and results in a forced convection flow over the rib section. In Figure 4A, a parallel flow channel is used on the cathode side. Since the two adjacent channels have the same geometric and inlet conditions, the pressure difference between the two channels is negligible and unable to create flow over the rib. However, in Figure 4B, using the interdigitated flow channel (Type I) on the cathode side, there is a large pressure difference between the two adjacent channels of the cathode. This pressure difference creates a strong cross flow between the two channels in the region under the rib. In Figure 4C,D, we show the streamlines for the interdigitated flow channels of type II and type III. Using the interdigitated flow channel of type II results in a zigzag transverse motion between the two adjacent cathode channels. However, in the case of the interdigitated flow channel type III, this zigzag transverse motion is different. In this channel geometry, the flow passing from the blocked channel is directed transversely into the adjacent channel, where it is merged with the incoming flow. Then, only after half of the channel length, the combined flow is directed to the fuel cell outlet by over-rib flow.

Establishing an over-rib convection mechanism, as shown in Figure 4, can cause fundamental changes in the distribution of the gaseous reactants and produced liquid water in the fuel cell. To better describe the effects of over-rib convection, the contours of oxygen concentration and liquid water are shown in Figures 5 and 6.

Figure 5 shows the pressure contours at the gas diffusion layer and cathode catalyst layer interface (labeled as CCL/GDL) and in the x–z planes that cross the cathode gas channels at height $H_{ch}/2$ (labeled as ch). As can be seen in Figure 5A,B, the pressure distribution for the parallel flow field is similar and symmetrical for adjacent channels. In a parallel flow channel, the pressure always decreases uniformly over the cross-sections from inlet to outlet. Because of the symmetry of the pressure distribution, there is no local difference between the pressure values of the two cathode channels and therefore convection over the rib is negligible. But with the various types of interdigitated flow fields, the pressure distribution is not symmetrical. For the Type I interdigitated flow field shown in Figure 5C,D, closing the outlet of one of the two channels increases the pressure and creates a

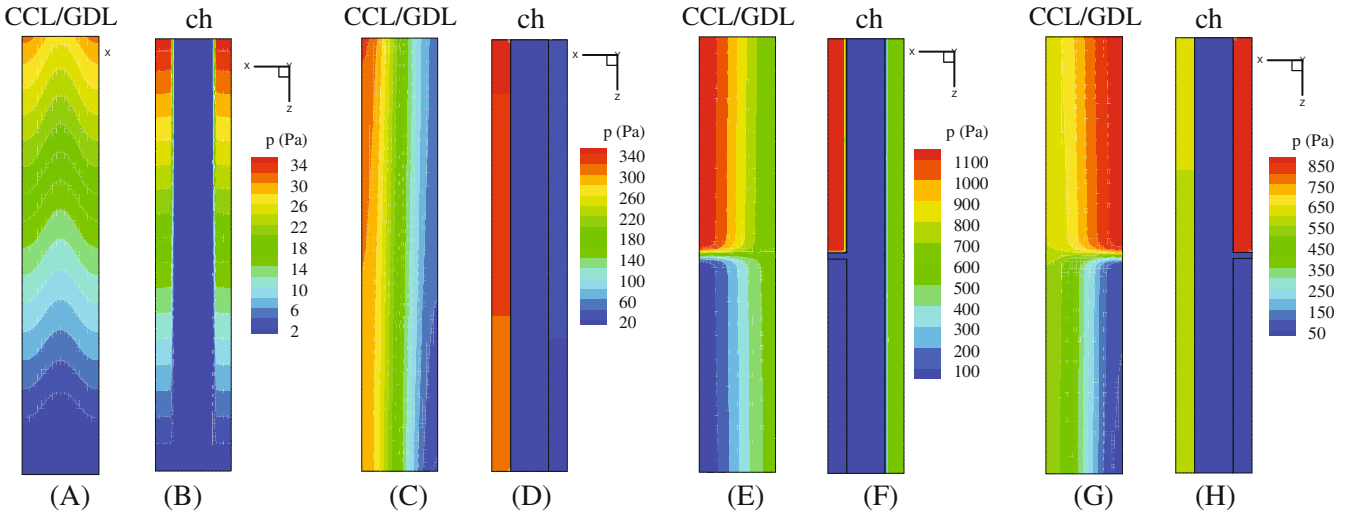

FIGURE 5 Pressure contours in x–z planes at the CCL/GDL interface (with constant y) and in x–z planes crossing the cathode channel at $H_{ch}/2$ for the flow fields: (A) and (B) parallel; (C) and (D) interdigitated type I; (E) and (F) type II; (G) and (H) type III

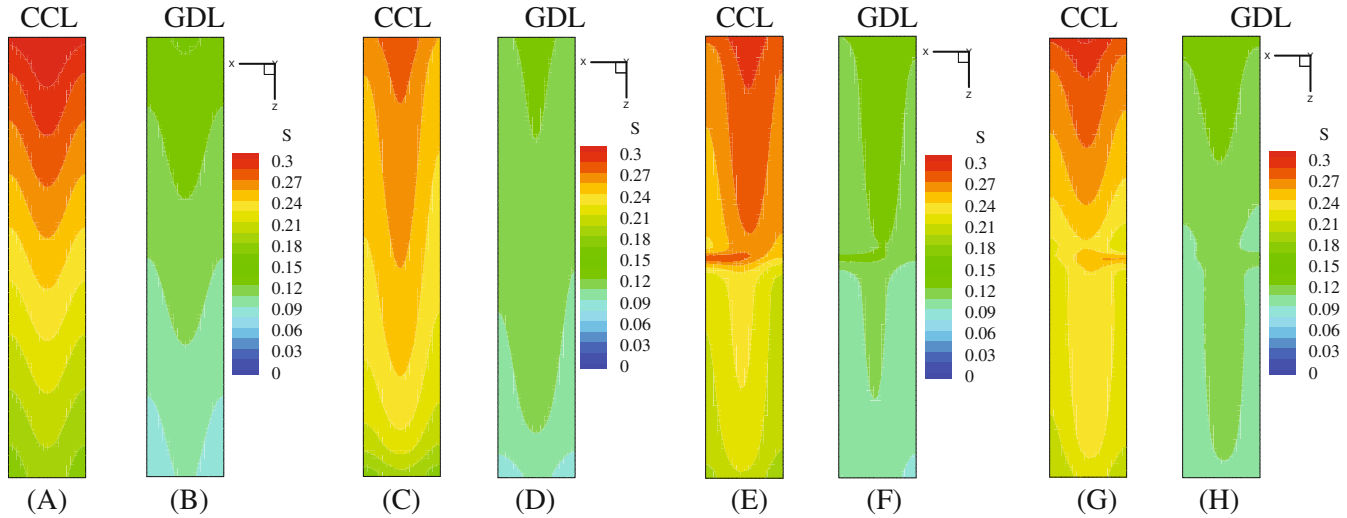

FIGURE 6 Distribution of liquid water saturation in the midplane of cathode gas diffusion and catalyst layers (x–z planes that cross the cathode gas diffusion layer at $H_{GDL}/2$ labeled as GDL and planes cross the cathode catalyst layer at $H_{CL}/2$ labeled as CCL) for the flow fields: (A) and (B) parallel; (C) and (D) interdigitated type I; (E) and (F) type II; (G) and (H) type III

pressure difference with the adjacent open outlet channel. In the interdigitated flow field type II (Figure 5E,F), different areas of the flow channel can be divided into three regions in terms of pressure. The channel shown on the left has an inlet, an intermediate block, and an outlet. The presence of a block causes the pressure at the beginning of this channel to increase. The adjacent channel (shown on the right) has no inlet or outlet and is fed by over-rib convection from the first half of the left channel. This region has a lower average pressure than the initial region of the left channel. The flow of reactants from this region is also directed to the end half of the left channel, which has the lowest pressure, due to the over-rib convection. In the interdigitated flow field type III (Figure 5G,H), which is similar to the interdigitated type II, three regions can be distinguished in terms of pressure. The main difference of the type III interdigitated flow field is that in the flow channel, where there is no obstacle, a pressure variation from the inlet to the outlet region is observed and the pressure drop is generally lower than in the flow channel of type II.

Figure 6 shows the contours of liquid water at various x–z planes that cross the cathode gas diffusion layer at height $H_{GDL}/2$ (labeled as GDL in Figure 6) and x–z planes cross the cathode catalyst layer at height $H_{CL/2}$ (labeled as CCL in Figure 6). Values greater than 0.1

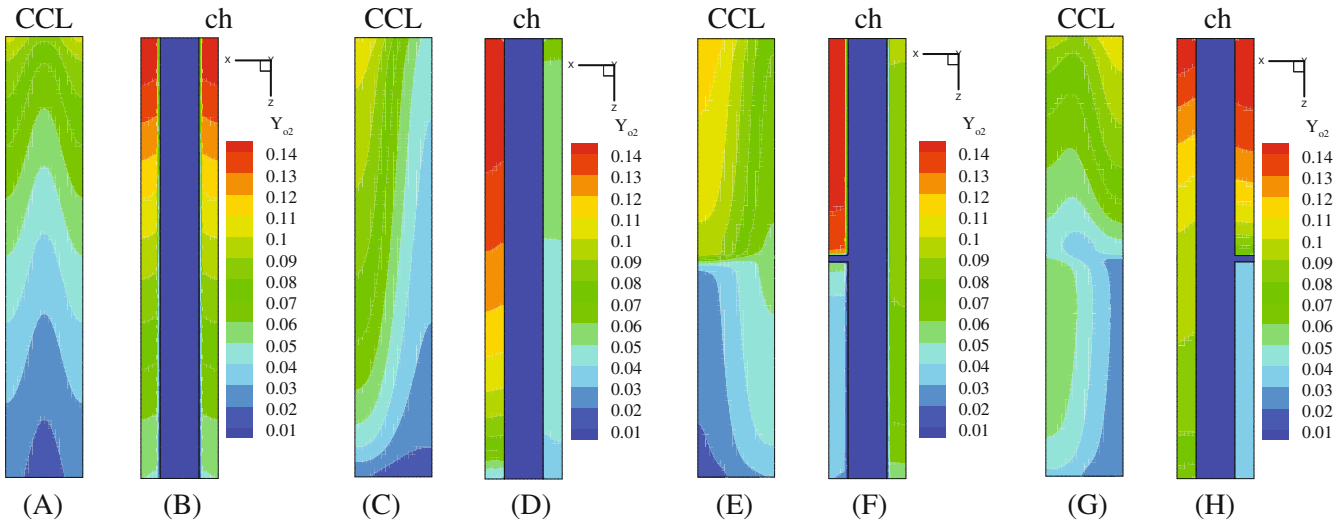

FIGURE 7 Contours of O_2 concentration in different x–z planes that cross the cathode catalyst layer at $H_{CL}/2$ labeled as CCL and planes cross the cathode channel at $H_{ch}/2$ labeled as ch for the flow fields: (A) and (B) parallel; (C) and (D) interdigitated type I; (E) and (F) type II; (G) and (H) type III

indicate the locations where the probability of flooding is higher due to the accumulation of liquid water. In all flow fields, liquid water accumulates below the rib area. It should be noted that the results shown in this figure correspond to a constant current density of 1 A/cm^2. Otherwise at a constant operating voltage, the average electrochemical reaction rate and consequently water production rate in the cathode catalyst layer would be the same for all the flow fields. Figure 6 clearly shows that the incorporation of interdigitated flow channels leads to a significant reduction of the amount of liquid water in the catalyst and the GDL. Such reduction in the amount of liquid water facilitates the transfer of reactants to the cathode catalyst layer and attenuates the mass transport overpotential in the fuel cell.

For the parallel flow field (Figure 6A,B), the water distribution is symmetrical about the cell midline and the highest amount of water is detected below the rib area and near the inlet, where the electrochemical reaction rate is higher. Also, the amount of liquid water collected in the catalyst layer is higher than in other the fuel cell components. We note that the amount of liquid water in the flow channel is insignificant due to the drag applied by the gas flow, implying that the liquid water is removed from the fuel cell by the gas flow itself. For the type I interdigitated flow field (Figure 6C,D), the contour of the liquid water distribution shows that the symmetry of the liquid water distribution is lost due to the over-rib component of the flow. For the second type of interdigitated flow channel (Figure 6E,F), there is also an accumulation of liquid water in the first half of the flow channel (upstream of the block) due to the higher reaction rate. In the case of the interdigitated flow channel of the type III (Figure 6G,H), the accumulation of liquid water is also observed in the first part.

The distribution of oxygen concentration in the different x–z planes is shown in Figure 7. These results indicate that when the parallel flow field is used, the oxygen concentration is highest precisely in the regions below the flow channels and the lowest O_2 concentration is seen in the regions below the rib. For the parallel flow channels, the convection effects over the ribs are negligible, and the transfer of reactants to the catalyst layer often occurs due to the diffusion mechanism and concentration gradient. However, for all types of interdigitated flow fields, the effect of convection over the ribs is significant leading to an increase of the oxygen concentration under the rib.

The local current density in the middle plane of the catalyst layer of the cathode (x–z planes that cross the cathode catalyst layer at height $H_{CL}/2$) is shown in Figure 8. For the parallel case, the highest local current density in the catalyst layer occurs at the locations below the flow channel. Also for this flow channel, the current density attains higher values in the regions close to the inlet and then decreases along the channel. For a type I interdigitated flow channel, the current density increases due to the forced convection of oxygen into the catalyst layer, implying higher current density in the rib region than in the parallel case. In the case of the interdigitated flow channel of type II, the increase in current density is much more pronounced. In the first half (before the position of the block), a higher local current density is generated in the rib region compared to the type I

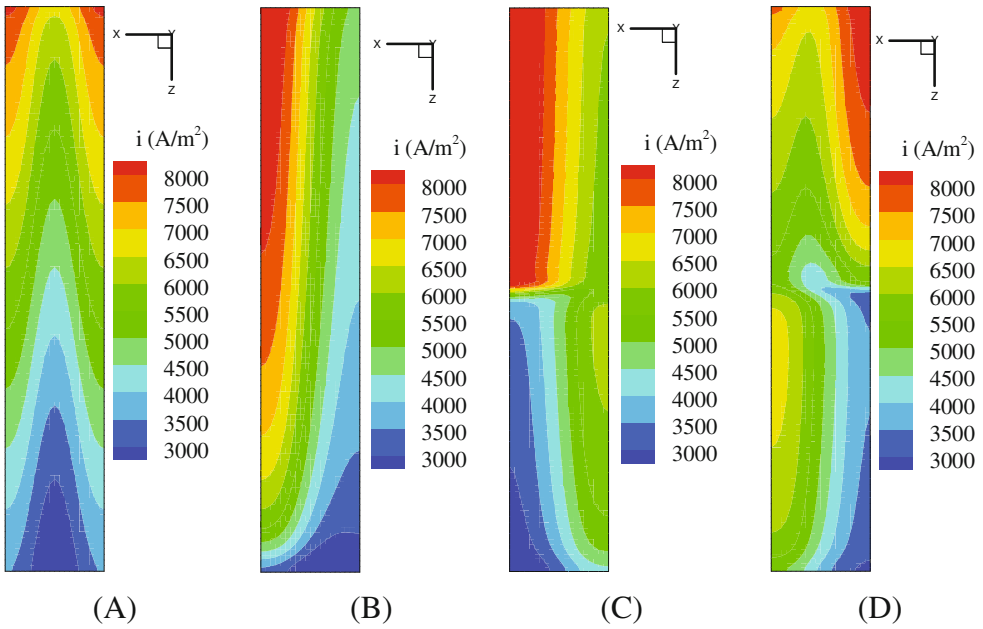

FIGURE 8 Contours of the local current density in x–z cross sections of the cathode catalyst layer (x–z planes that cross the cathode catalyst layer at $H_{CL}/2$) for the flow fields (A) parallel; (B) interdigitated type I; (C) type II; (D) type III

interdigitated flow field. In the third type interdigitated flow field, the local current density is lower than in the first and second types of interdigitated flow field because of the two inlets and the reduction of the flow over the ribs. Due to the presence of a block in the channel, the over-rib flow created near this channel causes a higher current density in the first half of the channel compared to the local values of the current for the adjacent channel. In the second half (after the block), the entire reactant flow from the channel where there is no intermediate blocking is transferred to the adjacent channel. This enhancement of mass transfer results in a higher local current density in this region.

To better demonstrate the mechanism of over-rib convection in different flow fields, three planes are considered in the z-direction, one of which passes through the location of the middle block ($Z2 = L_{ch}/2 = 35$ mm) and the other two planes are located at the beginning of the channel ($Z1 = L_{ch}/4 = 17.5$ mm, before the location of the block) and at the end of the channel ($Z3 = 3L_{ch}/4 = 52.5$ mm, after the location of the block). The transverse velocity vectors and the contours of the transverse velocity magnitude $V_{x-y} = \sqrt{u_{g,x}^2 + u_{g,y}^2}$ in different x–y sections for the parallel flow field and different types of interdigitated flow fields are shown in Figures 9 and 10, respectively.

For all flow fields shown in Figure 9, a forced convection flow over the rib can be seen on the anode side which uses a type I interdigitated flow field. Figure 9A-C clearly shows that there is no flow over the rib for the parallel flow field on the cathode side. However, with the type I interdigitated flow field (Figure 9D-F), there is a uniform over-rib flow along the channel from right to left. This over-rib flow is practically parallel to the over-rib flow on the anode side. In the second type of interdigitated flow field (Figure 9G-I), there is an over-rib flow from right to left at the beginning of the channel (region Z1). This cross-rib flow is stronger than that observed for the type I interdigital flow field (see Figure 10). In the obstruction zone (Z2), the cross-rib flow becomes weak and its direction reverses after the blockage (region Z3) and the over-rib flow occurs from left to right. In the case of the interdigitated flow field of type III (Figure 9J-L), the over-rib flow is initially generated from left to right. A comparison of the velocity vectors and the velocity contours in this region (Z1) shows that the crossflow in region Z1 is weaker in the interdigitated flow field of type III than in the flow fields of type I and II. In type III flow field, the direction of the over-rib flow reverses on the block. This over-rib flow, which is opposite to that from right to left (see above), is slightly more intense than the over-rib flow at the same location in the interdigitated type II flow field. After the block (region Z3), the intensity of the over-rib convection increases for the interdigitated flow field of type III.

In Figure 10, the contours of cross-wise velocity magnitude are shown for various flow fields and at three different cross sections of Z1, Z2, and Z3. For the parallel flow field, only a weak over-rib convection is observed at the another side. The intensity of this over-rib convection flow slightly reduces along the channel moving from cross section Z1 (Figure 10A) to cross section Z3 (Figure 10C). For the interdigitated flow field type, I (Figure 10D-F), the intensity of the over-rib convection in the cathode side is much higher than the over-rib convection flow in the anode side. This

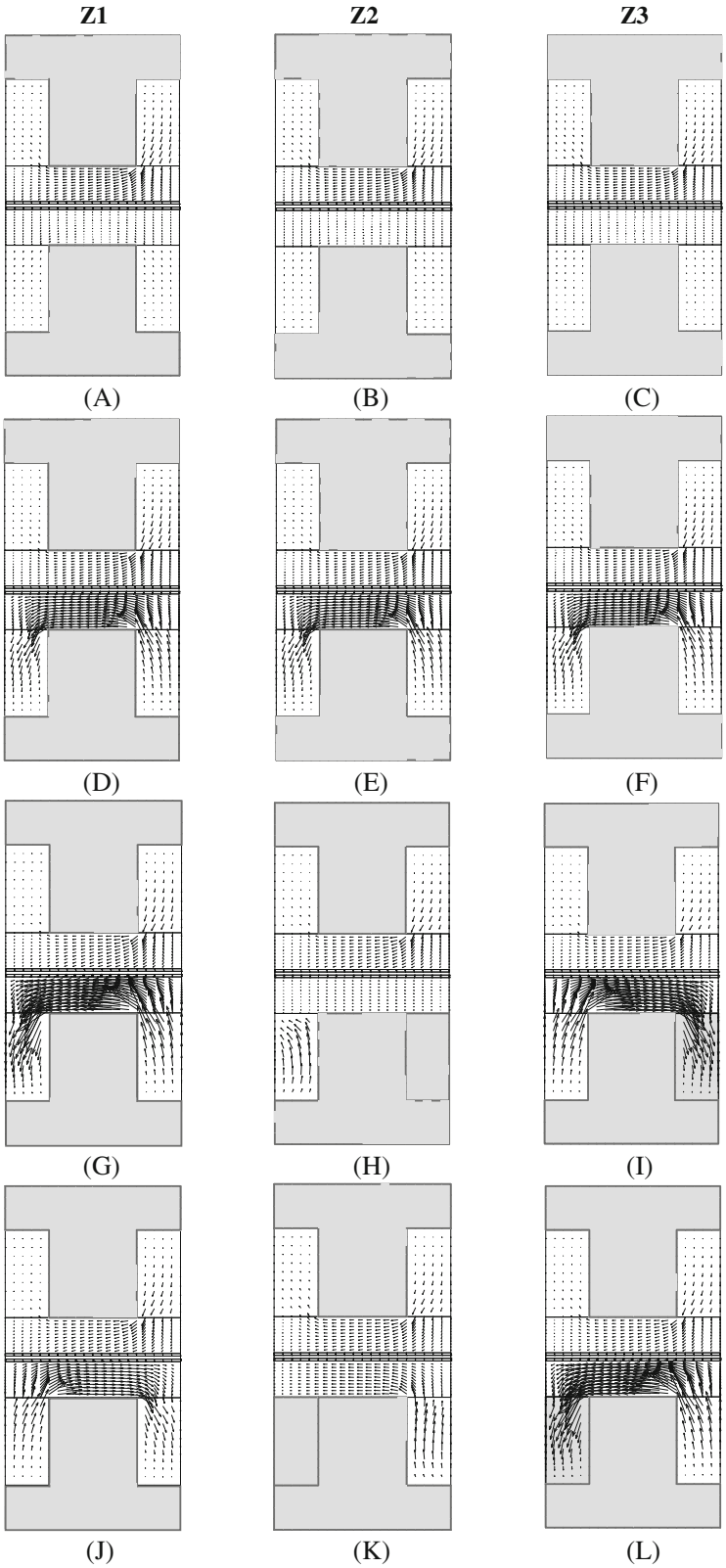

FIGURE 9 Cross-wise velocity vector plots in different x–y planes for the flow fields: (A), (B), and (C) parallel; (D), (E), and (F) interdigitated type I; (G), (H), and (I) type II; (J), (K), and (L) type III

induced over-rib convection almost maintains its intensity along the channel. For the type II flow field (Figure 10G-I), the intensity of the induced cross-wise velocity is increase both in the first half (Figure 10G) and second half of the channel (Figure 10I). This over-rib convection flow was observed to be stronger in the first half of the channel. For the type III flow field (Figures 10J-L), the induced over-rib convection in the

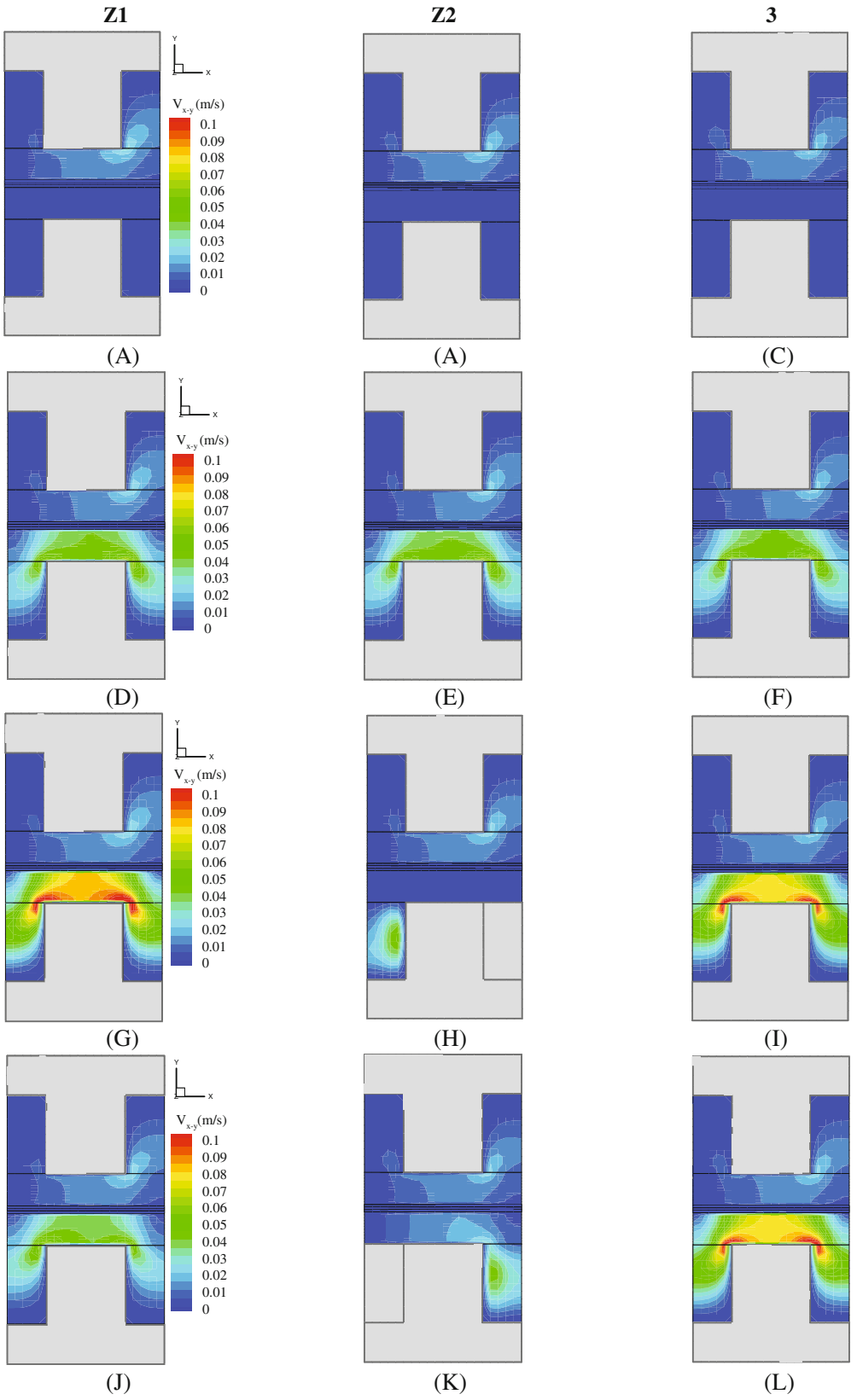

FIGURE 10 Contours of cross-wise velocity magnitude V_{x-y} in various x–y planes for the flow fields: (A), (B) and (C) parallel; (D), (E) and (F) interdigitated type I; (G), (H) and (I) type II; (J), (K) and (L) type III flow

first half of the channel (Figure 10J) had almost the same intensity as the type I flow field. However, the over-rib convection flow for the type III flow field was enhanced in the second half of the channel.

The amount of liquid water in different cross sections of the fuel cell with different flow fields is shown in Figure 11. In this figure, the values of liquid water saturation below 0.11 are not shown to better demonstrate the effect

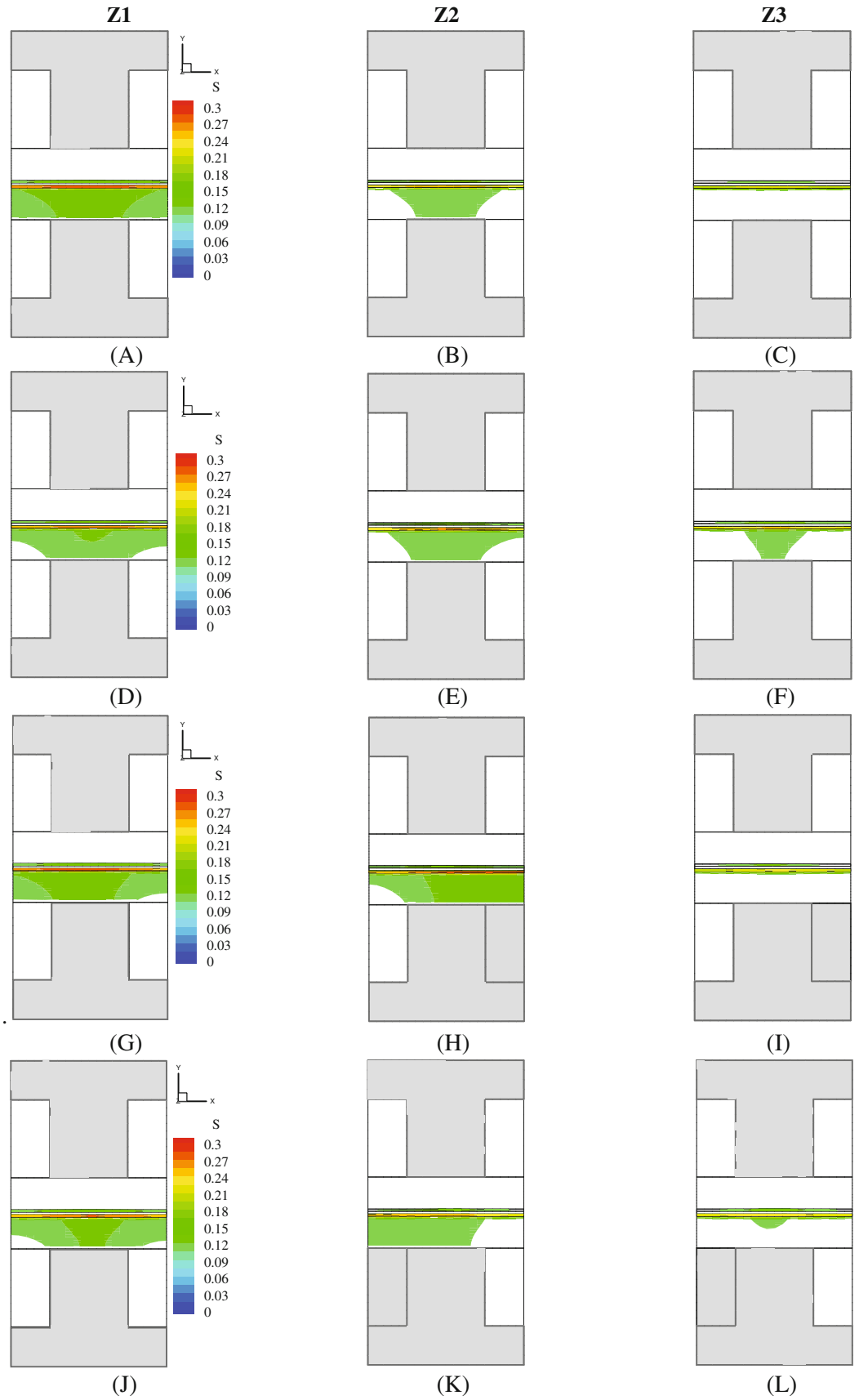

FIGURE 11 Contours of liquid water in various x–y planes at constant current density of 1 A/cm^2 for the flow fields: (A), (B), and (C) parallel; (D), (E), and (F) interdigitated type I; (G), (H), and (I) type II; (J), (K), and (L) type III

TABLE 6 Average values of mass fraction of oxygen in the catalyst layer and at the outlet, the pressure drop, the pumping power and the maximum net power density for all flow fields at constant voltage of $V = 0.25$ V

	Δp (Pa)	$P_{\text{pumping}}\left(\frac{\text{mW}}{\text{cm}^2}\right)$	$P_{\text{net}}\left(\frac{\text{mW}}{\text{cm}^2}\right)$	Y_{O_2}	$Y_{O_2,\text{out}}$
Parallel	36	0.04	320.27	0.0467	0.0479
Interdigitated type I	351	0.402	340.80	0.0545	0.0355
Interdigitated type II	1213	1.35	360.59	0.0617	0.0292
Interdigitated type III	757	0.844	349.22	0.0548	0.0345

of flow field on liquid water. As shown in Figure 11A-C, for the parallel flow channel at the beginning of the channel (Figure 11A, Z1 region), the cathode gas diffusion and catalyst layers are filled with liquid water. The accumulation of liquid water in the direction of the flow channel decreases, so that in the regions at the end of the channel (region Z3, Figure 11C), the amount of liquid water accumulated under the rib in the GDL (not in the catalyst layer) reaches less than 0.11. In the case of the type I interdigital flow field (Figure 11D-F), the liquid water in the first half of the channel was discharged from a part of the space of the GDL near the channels due to convection over the ribs. In the first half of the interdigitated flow channel type II (Figure 11G), some liquid water is removed from the regions near the inlet channel. But in the middle of the channel (regions above the block in Figure 11H), the accumulation of liquid water has increased compared to the previous two cases, and at the end (Figure 11I), the liquid water is completely discharged from the GDL. In the case of the interdigitated flow channel of type III (Figures 11J-L), the least amount of liquid water accumulation is observed in the initial part of the channels (Figure 11J) compared to the other flow fields. Similarly, to the type II interdigitated flow field, liquid water accumulation also occurs in the zone above the block (Figure 11K), and in the regions near the end of the channel, a small amount of liquid water is visible in the GDL.

For a more detailed and quantitative comparison of parallel flow channels and different types of interdigitated flow fields, the average values of the pressure difference between inlet and outlet (Δp), the average O_2 concentration in the catalyst layer (Y_{O_2}) and the average O_2 concentration at the outlet ($Y_{O_2,\text{out}}$) for a constant voltage of $V = 0.25$ V are given in Table 6. In addition, the parasitic pumping power density (P_{pumping}) and the maximum net power density (P_{net}) of the PEM fuel cell for the various flow fields are given in Table 6. The results show that the pressure drops in the interdigitated type I, II, and III flow fields are approximately 10, 33, and 21 times higher than in the parallel flow field, respectively. This increase in pressure drop is undesirable because it increases pumping power. In Table 6, the values of net output power density $P_{\text{net}} = VI - P_{\text{pumping}}$ and pumping power are also given. The corresponding

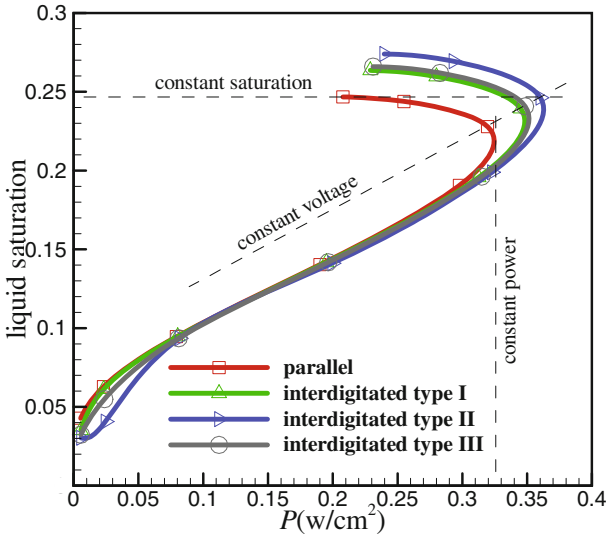

FIGURE 12 Volume fraction of liquid water vs fuel cell power density for the various flow fields

pumping power is calculated using $P_{\text{pumping}} = Q \times \frac{\Delta p}{\eta_p A_{cell}}$ where Q is the inlet volume flow rates and the A_{cell} is the active area of the cell and $\eta_p = 85\%$ is the pumping efficiency. We should mention that the required mass flow for the single cell is also small and therefore the resulting pumping power was small and did not affect the generated power significantly. However, for a stack of fuel cells, the values of pressure drop will be much higher and will influence the overall efficiency of the fuel cell. If the pressure drop is increased for a fuel cell stack, the compressor used to deliver the air to the cathode side will require a higher power and thus it will add additional cost to the system or even the size of this compressor may be larger. In addition, higher pressure drop in the cathodic gas channels may cause unwanted pressure difference over the membrane and thus result in higher rates of cross-over leading to performance drop. The results in Table 6 show that, the mass fraction of O_2 in the catalyst layer is larger for interdigitated flow fields than for the parallel flow field. The results also show that among the interdigital flow fields, the type II provides the largest mass fraction of oxygen in the catalyst layer. In fact, the mass fraction of oxygen had the highest value in the interdigitated field of the second type, followed by the third type and the first type. The mass fraction of

oxygen at the outlet of the cathode flow channel reported in Table 6 indicates that the reactant was better utilized, that is, the reactant (here, the oxygen) was consumed more efficiently in the catalyst layer.

Figure 12 shows the results of liquid water saturation vs fuel cell power density, for the various cathode flow fields. The plots shown in this figure can be viewed from two perspectives. In the first case, the resulting fuel cell power density is considered constant (meaning that the output current density and consequently the reactant consumption and water production rate are constant). In this first case, the flow field that results in less average liquid water saturation is more capable of repelling liquid water from the fuel cell. In the second view, we can consider the condition that the amount of liquid water in the fuel cell is constant. In this case, the higher output power density means that the flow field has more effectively increased the transfer rate of reactants to the catalyst layer. As seen in Figure 12, when the power density is constant (eg, is the maximum power density produced with a parallel flow field), there is less liquid water in the interdigitated flow fields. When the power density is constant (less than or equal to the maximum power density of the parallel case), Figure 12 shows that the second, third, and first types of interdigitated flow field have the best performance in repelling liquid water. Finally, if we consider a constant liquid water saturation (equal to 0.25, as shown by the horizontal dashed line in Figure 12), we see that among the various flow fields the interdigitated flow channel type II produces the highest electrical power, thus indicating an improvement in the transfer of reactants to the catalyst layer.

6 | CONCLUSION

In this paper, a comparison is made between the performance of a conventional interdigitated flow field without intermediate block (type I) and interdigitated flow fields (with middle block) of type II and type III. Based on the numerical simulation results, an analysis of the V–I curves, velocity, pressure, and O_2 concentration contours, and liquid water saturation distribution in the catalyst layer was performed. Also, the average values of the mass fraction of O_2 in the catalyst layer and the pressure drop were given for a better comparison of the different flow fields. The main results of this paper can be summarized as follows:

- From the comparison of the polarization curves at reference conditions, it is concluded that all types of interdigitated flow fields produce higher maximum power than the parallel flow field. The positive effect of the interdigitated flow fields compared to the parallel flow field occurs at current densities greater than 0.6 A/cm^2 when concentration losses predominate. Among the interdigitated flow fields, the type II results in the largest limiting current density and the highest output power density; Moreover, compared with the type I interdigitated flow field, the type III slightly increases the fuel cell performance in terms of limiting current density and output power density. The results indicate that the type I, II, and III interdigitated flow fields lead to an increase of the limiting current density (corresponding to an operating voltage of 0.2 V) of 10.6%, 15.6%, and 11.4%, respectively, compared to the parallel flow field. In addition, the results for the reference conditions show that the interdigitated flow field of types I, II, and III also increased the maximum net output power density of the fuel cell by 8.2%, 12.6%, and 9.0%, respectively, compared to the parallel flow field. Hence, for both properties, type II arrangement achieves the best performance.
- The comparison of the pressure difference between the inlet and outlet of the flow channels shows that this pressure drop increases significantly in all interdigitated flow fields compared to the parallel flow field, as expected. For the type I, II, and III interdigitated flow fields, the pressure drop is about 10, 34, and 21 times higher than the pressure drop of the parallel flow field. Hence, the interdigitated flow field of type II requires the largest pumping power and the type I has the smallest pumping power.
- By analyzing the distribution of pressure, velocity, O_2 concentration, and liquid water saturation, it is found that interdigitated flow fields greatly increase the O_2 concentration in the catalyst layer. In addition, more liquid water was expelled from the catalyst layer by the interdigitated flow fields than by the parallel flow field. Overall, improved transfer of reactants to the reaction site and improved removal of liquid water due to induced convection flow are the two main reasons for the improvement in fuel cell performance of interdigitated flow fields compared to the parallel flow field. Among interdigitated flow fields, the type II shows an increase of 13.2% in the average mass fraction of oxygen in the catalyst layer compared to the type I interdigitated flow field, due to intensification of convection flow over the ribs at both the beginning and end of the flow channel. Analysis of the plots of liquid saturation vs power density shows that for a given power density, the amount of liquid water that accumulates in the catalyst layer is lower for the interdigitated flow field of type II compared to type I and III flow fields.

NOMENCLATURE

A	Area (m^2)
a	Water activity
a_{pt}	Effective specific surface area (m^{-1})
C	Molar concentration (mol m^{-3})
D_{gl}	Rate constant of the evaporation /condensation phase change (m^2 s^{-1})
D_{liq}	Diffusion coefficient of liquid water in flow channels (m^2 s^{-1})
D_k	Diffusion coefficient of species at specified pressure and temperature (m^2 s^{-1})
D_w^{mem}	Effective diffusion coefficient of dissolved water in the membrane (m^2 s^{-1})
E_i^k	Reaction activation energy (J $kmol^{-1}$)
EW	Equivalent weight of dry membrane (kg mol^{-1})
F	Faraday constant (96 487 C mol^{-1})
h	Measure of grid spacing (m)
I	Current density (A m^{-2})
$\vec{i}_m$	Ionic current density in the membrane (A m^{-2})
$J(S)$	Leveret function
$j_{O_2}^{\text{ideal}}$	Ideal oxygen consumption rate in the cathode catalyst layer (mol m^{-2} s^{-1})
$j(T)$	Reference transfer current per unit area as a function of temperature (A m^{-2})
K	Absolute permeability of porous media (m^2)
K_{rl}	Relative permeability of liquid
K_wD_w	Solubility of oxygen in liquid water (m^2 s^{-1})
M_k	Molecular weight of species k (kg mol^{-1})
$\dot{m}$	Mass flow rate (kg s^{-1})
n_d	Electroosmotic drag coefficient
p_c	Capillary pressure (Pa)
p	Pressure (Pa)
R	universal gas constant (8.314 J mol^{-1} K^{-1})
R_{an}, R_{ca}	Anode and cathode exchange current density (A m^{-3})
R_{sol}, R_{mem}	Electronic and protonic exchange current density (A m^{-3})
$\mathfrak{R}_{\text{liq}}$, $\mathfrak{R}_{\text{ion}}$	Mass transfer resistance due to liquid water and ionomer in the catalyst agglomerates (S m^{-1})
r_{agg}	Agglomerate diameter (m)
S	Liquid water saturation
S_k, S_m	Source/sink terms for the specious conservation and continuity equations (kg m^{-3} s^{-1})
S_u	Source/sink terms for the momentum equation (kg m^{-2} s^{-2})
S_{gd}, S_{ld}, S_{gl}	The phase change rate between: water vapor and dissolved water, liquid water and dissolved water, water vapor and liquid water (kg m^{-3} s^{-1})
S_λ	Source/sink terms for the dissolved water (kg m^{-3} s^{-1})
T	Absolute temperature (K)
t	Time (s)
$\vec{u}_g$	Gas phase velocity (m s^{-1})
V	Voltage (Volt)
Y_k	Mass fraction of a chemical species

Greek letters

α	Charge transfer coefficient
γ_e, γ_c	Evaporation/condensation rate constants (m^{-2})
γ_{gd}, γ_{ld}	Liquid to dissolved phase mass transfer rate constants (s^{-1})
Δp	Pressure drop (Pa)
ε	Porosity coefficient
ε_{mem}	Volume fraction of a Nafion polymer
η	Over-potential (Volt)
θ_c	Contact angle (degree)
λ	Membrane water content
μ	Dynamic viscosity (Pa s)
ξ	Stoichiometric coefficient
ρ	Density (kg m^{-3})
σ	Surface tension of liquid water (N m^{-1})
σ_{sol}	Electronic conductivity (S m^{-1})
σ_{mem}	Proton conductivity (S m^{-1})
τ	Stress tensor (kg m^{-2} s^{-2})
ϕ_{sol}, ϕ_{mem}	Electric potential of solid/membrane phase (V)
χ	Ratio of liquid flow to gas flow velocity

Subscripts/superscripts

an	anode
bp	bipolar plate
ca	cathode
eff	effective
equil	equilibrium
g	gas
l	liquid
mem	membrane
oc	open-circuit potential
ref	reference
sat	saturation
wv	water vapor

Abbreviations

ACL	anode catalyst layer
CCL	cathode catalyst layer
ch	channel
CL	catalyst layer
GDL	gas diffusion layer
mem	membrane

ACKNOWLEDGEMENTS

The financial support received by FCT Project CEECIND/03347/2017 and by Portuguese national funds also from FCT - Foundation for Science and Technology, I.P., within the unit C-MAST - UIDB/00151/2020 are acknowledged by the authors.

DATA AVAILABILITY STATEMENT

The data that support the findings of this study are available from the corresponding author upon reasonable request.

ORCID

Fatemeh Bagherighajari https://orcid.org/0000-0003-0654-4458
Abbas Ramiar https://orcid.org/0000-0003-0777-2778
Mohammadmahdi Abdollahzadehsangroudi https://orcid.org/0000-0002-9396-3855
José Carlos Páscoa https://orcid.org/0000-0001-7019-3766
Paulo J. Oliveira https://orcid.org/0000-0001-9843-7558

REFERENCES

1. Havaej P, Kermani MJ, Abdollahzadeh M, Heidary H, Moradi A. A numerical modeling study on the influence of catalyst loading distribution on the performance of polymer electrolyte membrane fuel cell. *Int J Hydrog Energy*. 2018;43(21):10031-10047.
2. Abdollahzadeh M, Pascoa JC, Ranjbar AA, Esmaili Q. Analysis of PEM (polymer electrolyte membrane) fuel cell cathode two-dimensional modeling. *Energy*. 2014;68:478-494.
3. Hamrang A, Abdollahzadeh M, Kermani MJ, Rahgoshay SM. Numerical simulation of the PEM fuel cell performance enhancement by various blockage arrangement of the cathode serpentine gas flow channel outlets/inlets. *Int J Heat Mass Transf*. 2022;186:122475.
4. Limjeerajarus N, Santiprasertkul T. Novel hybrid serpentine-interdigitated flow field with multi-inlets and outlets of gas flow channels for PEFC applications. *Int J Hydrog Energy*. 2019;45(25):13601-13611.
5. Arvay A, French J, Wang JC, Peng XH, Kannan AM. Nature inspired flow field designs for proton exchange membrane fuel cell. *Int J Hydrog Energy*. 2013;38(9):3717-3726.
6. Kazim A, Forges P, Liu HT. Effects of cathode operating conditions on performance of a PEM fuel cell with interdigitated flow fields. *Int J Energy Res*. 2003;27(4):401-414.
7. Nguyen TV, He W. Interdigitated flow field design. *Handbook of Fuel Cells*. Hoboken, New Jersey: John Wiley & Sons, Ltd; 2010.
8. Ramiar A, Mahmoudi AH, Esmaili Q, Abdollahzadeh M. Influence of cathode flow pulsation on performance of proton exchange membrane fuel cell with interdigitated gas distributors. *Energy*. 2016;94:206-217.
9. Ding Q, Zhao H-L, Wan Z-M, Yang Y-R, Yang C, Wang X-D. Performance of parallel, interdigitated, and serpentine flow field PEM fuel cells with straight or wavelike channels. *J Energy Eng*. 2020;146(5):04020054.
10. Fei JQ, Qing MG, Liang QX. Influences of gas relative humidity on the temperature of membrane in PEMFC with interdigitated flow field. Renew. *Energy*. 2014;62:129-136.
11. Cooper NJ, Smith T, Santamaria AD, Park JW. Experimental optimization of parallel and interdigitated PEMFC flow-field channel geometry. *Int J Hydrog Energy*. 2016;41(2):1213-1223.
12. Huang Z, Xing L, Tu Z. Performance improvement in a proton exchange membrane fuel cell with an innovative flow field design. *Int J Energy Res*. 2022;46(5):6623-6636.
13. Wang C, Zhang Q, Shen S, Xiaohui Y, Zhu F, Cheng X. The respective effect of under-rib convection and pressure drop of flow fields on the performance of PEM fuel cells. *Sci Rep*. 2017;7:43447.
14. Kanezaki T, Li X, Baschuk JJ. Cross-leakage flow between adjacent flow channels in PEM fuel cells. *J Power Sources*. 2006;162(1):415-425.
15. Jiao K, Bachman J, Zhou Y, Park JW. Effect of induced cross flow on flow pattern and performance of proton exchange membrane fuel cell. *Appl Energy*. 2014;115:75-82.
16. Yin Y, Wang X, Zhang J, Shangguan X, Qin Y. Influence of sloping baffle plates on the mass transport and performance of PEMFC. *Int J Energy Res*. 2019;43(7):2643-2655.
17. Heidary H, Kermani MJ, Dabir B. Influences of bipolar plate channel blockages on PEM fuel cell performances. *Energy Convers Manag*. 2016;124:51-60.
18. Zhang X, Yang X, Gao W, Wang C. An experimental research on the net output power and current density distribution of PEM fuel cells with trapezoid baffled flow fields. *Int J Energy Res*. 2021;45(15):21464-21475.
19. Heidary H, Kermani MJ, Prasad AK, Advani SG, Dabir B. Numerical modelling of in-line and staggered blockages in parallel flowfield channels of PEM fuel cells. *Int J Hydrog Energy*. 2017;42(4):2265-2277.
20. Li WZ, Yang WW, Wang N, Jiao YH, Yang Y, Qu ZG. Optimization of blocked channel design for a proton exchange membrane fuel cell by coupled genetic algorithm and three-dimensional CFD modeling. *Int J Hydrog Energy*. 2020;45(35):17759-17770.
21. Yan W, Mei S, Soong C, Liu Z, Song D. Experimental study on the performance of PEM fuel cells with interdigitated flow channels. *J Power Sources*. 2006;160(1):116-122.
22. Thitakamol V, Therdthianwong A, Therdthianwong S. Mid-baffle interdigitated flow fields for proton exchange membrane fuel cells. *Int J Hydrog Energy*. 2010;36(5):3614-3622.
23. Wang L, Husar A, Zhou T, Liu H. A parametric study of PEM fuel cell performances. *Int J Hydrog Energy*. 2003;28(11):1263-1272.
24. Abdollahzadeh M, Ribeirinha P, Boaventura M, Mendes A. Three-dimensional modeling of PEMFC with contaminated anode fuel. *Energy*. 2018;152:939-959.
25. Zamel N, Li X. Non-isothermal multi-phase modeling of PEM fuel cell cathode. *Int J Energy Res*. 2010;34(7):568-584.
26. Yun W, Wang C-Y, Chen KS. Elucidating differences between carbon paper and carbon cloth in polymer electrolyte fuel cells. *Electrochim Acta*. 2007;53(12):3965-3975.

27. Wu H, Li X, Berg P. On the modeling of water transport in polymer electrolyte membrane fuel cells. *Electrochim Acta*. 2009;54(27):6913-6927.
28. Springer TE, Zawodzinski TAGS. Polymer electrolyte fuel cell model. *J Electrochem Soc*. 1991;138:2334-2342.
29. Ye Q, Van Nguyen T. Three-dimensional simulation of liquid water distribution in a PEMFC with experimentally measured capillary functions. *J Electrochem Soc*. 2007;154(12):B1242-B1251.
30. Kulikovsky AA, Divisek J, Kornyshev AA. Modeling the cathode compartment of polymer electrolyte fuel cells: dead and active reaction zones. *J Electrochem Soc*. 1999;146(11):3981-3991.
31. Mazumder S, Cole JV. Rigorous 3-D mathematical modeling of PEM fuel cells II. Model predictions with liquid water transport. *J Electrochem Soc*. 2003;150(11):A1510-A1517.
32. Um S, Wang C-Y, Chen KS. Computational fluid dynamics modeling of proton exchange membrane fuel cells. *J Electrochem Soc*. 2000;147(12):4485.
33. Penga Ž, Bergbreiter C, Barbir F, Scholta J. Numerical and experimental analysis of liquid water distribution in PEM fuel cells. *Energy Convers Manag*. 2019;189:167-183.
34. Seidenberger K, Wilhelm F, Schmitt T, Lehnert W, Scholta J. Estimation of water distribution and degradation mechanisms in polymer electrolyte membrane fuel cell gas diffusion layers using a 3D Monte Carlo model. *J Power Sources*. 2011;196(12):5317-5324.
35. Sun W, Peppley BA, Karan K. An improved two-dimensional agglomerate cathode model to study the influence of catalyst layer structural parameters. *Electrochim Acta*. 2005;50:3359-3374.
36. Sasmito AP, Brigerson E, Mujumdar AS. Numerical investigation of liquid water cooling for a proton exchange membrane fuel cell stack. *Heat Transf Eng*. 2011;32(2):151-167.
37. ANSYS. Fluent Advanced Add-on Modules. 2016.
38. Roache PJ. Perspective: a method for uniform reporting of grid refinement studies. *J Fluids Eng*. 1994;116(3):405-441.
39. Celik IB, Ghia U, Roache PJ, Freitas CJ, Coleman H, Raad PE. Procedure for estimation and reporting of uncertainty due to discretization in CFD applications. *J Fluids Eng*. 2008;130(7):0780011.

How to cite this article: Bagherighajari F, Ramiar A, Abdollahzadehsangroudi M, Páscoa JC, Oliveira PJ. Numerical simulation of the polymer electrolyte membrane fuel cells with intermediate blocked interdigitated flow fields. *Int J Energy Res*. 2022;46(11):15309-15331. doi:10.1002/er.8233